Natural branching - inspired heat exchanger design for heat transfer enhancement

Chemical Engineering & Processing: Process Intensification 218 (2025) 110556

Contents lists available at ScienceDirect

Chemical Engineering and Processing - Process Intensification

journal homepage: www.elsevier.com/locate/cep

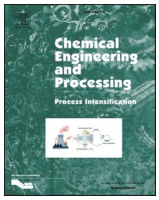

Natural branching - inspired heat exchanger design for heat transfer enhancement

Aladdin Mardanov, Ronnie Andersson, Jia Wei Chew *

Department of Chemistry and Chemical Engineering, Chalmers University of Technology, Gothenburg, 412 96, Sweden

ARTICLE INFO

Keywords:
Heat exchanger
Nature-inspired chemical engineering
Heat-transfer efficiency
Nature-evolved transport network
Green transition

ABSTRACT

The ubiquity of heat exchangers, coupled with the urgent need to augment energy efficiency in the green transition of industries, underscores the importance of optimizing the flow-field design to maximize heat transfer. Inspired by nature-evolved transport networks (e.g., tree branches), this study explores 3D three-level trifurcating pipe networks with varying branching angles (20° - 65°) as alternatives to conventional vertical pipes. Three key conclusions are highlighted. Firstly, steep temperature increases at junctions lead to distinctly different heat transfer and flow behaviors in the middle level among the geometries. Secondly, the relationship between the *Re*-normalized thermal performance factor (TPF) is non-monotonic with respect to angle, with the 36° model giving the highest TPF/*Re* value. Thirdly, the superior performance of the 36° model is associated with the lowest mean normalized turbulent viscosity (μ_t/Re) and highest mean normalized vorticity ($\Omega D/U$), suggesting the flow is dominated by coherent rotational strcutures rather than chaotic, dissipative turbulence. These coherent vortices could be leveraged - by judiciously mimicking the 36° configuration - to further enhance thermal performance. Furthermore, the difference in turbulent viscosity between the outer and central pipes in the top level is the least for the 36° model, indicating enhanced uniformity. These findings offer insights for designing efficient, nature-inspired heat exchangers.

1. Introduction

The ubiquity of heat exchangers coupled with the need to augment energy efficiency in the green transition of industries necessitates optimizing the flow-field design to significantly enhance the heat-transfer efficiency. Biomimicry of plants, animals, and nest structures for heat exchanger designs has consistently been acknowledged to give higher heat transfer and lower pressure drop, which translates to energy savings [1]. Thus, nature-evolved transport networks (e.g., leaf vein, lung) can provide valuable heuristics for heat transfer and flow distribution in heat exchangers [2]. While nature offers many examples of heat transfer means and flow networks that have been optimized through evolution, a straightforward imitation is potentially feasible. Correspondingly, a more systematic methodology based on in-depth mechanistic understanding, which thereby augments scalability and applicability, has proliferated [3]. Heat exchangers have not fully benefited from such systematic biomimicry of nature-optimized designs, which motivated the current study.

Natural flow and heat-exchange systems are often complex, much more so than the conventional unit operations in the industry. Some examples are the structures of flow patterns of any fluid (in free space, on surfaces, and closed systems), growth of fungus, vascular design of all living creatures, intricate networks of mycelium, flow pattern of electrons in air during lightning, and heat regulation in termite mounds. All of these evolved structures can provide blueprints for efficient, innovative engineering solutions. An interesting heat-exchanger example in nature is the vascular design of an elephant ear, which helps the mammal exchange heat efficiently to cool body temperature during high heat waves in tropic regions [4,5]. Another analogous example is asymmetric development of bifurcating arteries in humans, particularly in the lungs [6]. Blood flow is usually laminar in living organisms [6,7], but heat exchangers are typically operated in the turbulent regime. Nonetheless, these flow and heat-exchange designs that have been optimized by nature can be judiciously mimicked to address the urgent sustainability challenges, which is in part underpinned by augmenting energy efficiency [8].

Genetic algorithm was used to design microvascular networks in polymers that mimic the heating/cooling system of mammals [9]. Multi-scale networks with minimum flow maldistribution were designed for cooling systems in fields ranging from energy, chemicals manufacturing, and electronics [10]. Moreover, 3D distribution systems

* Corresponding author.
E-mail address: jia.chew@chalmers.se (J.W. Chew).

https://doi.org/10.1016/j.cep.2025.110556
Received 26 June 2025; Received in revised form 11 September 2025; Accepted 13 September 2025
Available online 15 September 2025

Nomenclature

β	Angle of a branch inclination over *xy* plane [degrees].	ΔP	Pressure drop [Pa]
D	Inner tube diameter [mm]	T	Temperature [K]
Nu	Nusselt number	μ_t	Turbulent viscosity [kg/ms]
Nu_o	Nusselt number of a conventional vertical pipe	ρ	Density of fluid [kg/m^3].
h	Heat transfer coefficient [W/m^{2}K]	U	Velocity magnitude [m/s]
k	Thermal conductivity of fluid [W/mK]	L	Length of a pipe [m]
j	Colburn j factor	Q	Q criterion [s^{-2}]
Re	Reynolds number	Ω	Vorticity tensor [s^{-1}]
Pr	Prandl number	S	Strain rate tensor [s^{-1}]
TPF	Thermal performance factor	ω_{ij}	Vorticity magnitude [s^{-1}]
f	Darcy-Weisbach friction factor	u	Velocity in x direction [m/s]
		v	Velocity in y direction [m/s]
		w	Velocity in z direction [m/s]

have been widely exploited in the oil and gas, pharmaceutical, and food industries for heat exchange [11]. Also, two-dimensional flow distribution models have been used to design shell-and-pipe heat exchangers [12–16], with one study focused on minimizing pressure drop [17]. There are other ways for heat transfer to be also improved by bioinspired surface structures [18–20], which enhances heat transfer coefficients due to the increase in flow resistance that these micro-structures generate [21]. The leaf architecture of vascular plants and tree branches that have been optimized over 400 million years for efficient water transport in various climates provide for an excellent basis for mimicry [22,23]. Leaf veins or tree branches are never parallel pipes, but systematically branched networks to minimize the cost of transporting water, carbon and nutrients in both hot and cold habitats. Branching pipe networks that mimic the vascular system have been reported to promote better fluid distribution and thus augment heat transfer [24], based on Bejan's fractal-based constructal theory that branching structures similar to that of trees aid to distribute fluids more uniformly [25] and also maximize heat transfer rate [26]. Specifically, Bejan's theory states that fractal systems satisfy certain aspect ratio that defines the proportions of the flow channels evolved to reduce resistance [27], which has been found to be inadequate for more complex systems [28], while adequate for others [15]. The fractal honeycomb reactor design has visible bifurcation patterns to increase the surface to volume ratio [29]. As for the angle of the branches, the optimized value has been reported to be 37.5° [30], or more broadly between 15° and 45° [31]. Perpendicular branching has been shown to be detrimental due to stagnation [16], while larger angle of branches has been tied to lower pressure drop [15]. All these provide valuable heuristics for the focus here on designing the natural branching - inspired heat exchangers.

To mimic such natural transport networks to maximize heat transfer efficiency in designing heat exchangers, the focus here was on the impact of branching angle, and the corresponding underlying mechanisms. Three-level, trifurcation 3D models were constructed for branching angles ranging between 20° and 65°. Benchmarked against a conventional vertical pipe, the heat transfer characteristics of the branched models were first explored, followed by the flow behaviors.

2. Simulation setup

The three-dimensional (3D) pipe networks were built using Autodesk Fusion 360. As depicted in Fig. 1a, the angles (β), defined with respect to the horizontal axis, investigated are 20°, 36°, 45° and 65°. As exemplified by the 3D setups for the trifurcation angles of 20° and 65°, respectively, in Fig. 1b and c, the total height of 540 mm was divided into three levels. Specifically, the bottom level is a vertical pipe, the level immediately above diverges into three pipes, and the level subsequently above further diverges into nine pipes. Each pipe has an inner diameter (D) of 48.6 mm, and the pipe length (l_{pipe}) within each branched model is kept constant (i.e., ranging between 178 – 297 mm). The height of each level differs among the different angled models. For each angle β, the height of each level is l_{pipe}·sin (β).

The built models were then imported to Ansys Fluent Workbench. The liquid that flows through the setups was water (density = 0.997 g/cm^3, viscosity = 0.97 mPa·s). Regardless of geometry, the mean residence time of the liquid in the setup was kept constant at 10.6 s, resulting in Reynolds numbers (Re) ranging between 3000 (for the top level of the 65° model) and 45,000 (for the bottom level of the 20° model), reflecting turbulent flow regimes. The boundary conditions were constant in all cases, with the inlet temperature set at 295.15 K, the wall temperature at 360 K and the outlet pressure at 101,325 Pa. Correspondingly, with respect to angle, the total heat supplied decreases monotonically due to the decrease in wall surfaces, and the mass flow

Fig. 1. (a) Schematic depicting the definition of angle of branches β. 3D models with the narrowest and widest trifurcation angles investigated for three-level designs with trifurcation angles of (b) 20° and (c) 65°. The total height was divided into three levels: the bottom level has 1 pipe, the middle level has 3 pipes, while the top level has 9 pipes. The inner diameter of each pipe (D) is 48.6 mm.

rate decreases monotonically to maintain the same residence time.

The k-omega ($k-\omega$ *SST*) turbulence model was employed for better near-wall modelling and viscous sublayer, and Pressure-Velocity coupling numerical scheme was selected as coupled with a Second Order Upwind spatial discretization to prevent numerical diffusion. Additional validation using PRESTO! was carried out due to the presence of bends in the geometry and swirling flows after junctions. Meshing was performed with poly-hexahedral meshes, due to the best mesh alignment and reduced diffusion in the viscous sub-layer, with prismatic inflation layers in the wall region (Fig. A1). The smallest and largest dimensions were pre-set respectively 0.2 μm and 10 mm, and the growth rate was set at 1.2 before mesh adaption. The total number of cells ranged between 2×10^5 (for the single vertical tube) and 8×10^6. Mesh refinement was performed for the wall boundary layer to limit the y^+ values for all models to less than 0.9.

The key parameters extracted from directly from Ansys include velocity in all three directions (i.e., *x*, *y*, and *z*), *Q* criterion, area-weighted Nusselt number (*Nu*), surface heat transfer coefficient (*h*), vorticity, helicity, pressure, and temperature.

Nu was calculated through custom field functions as follows:

$$Nu = \frac{h \cdot D}{k}$$

where *k* is the thermal conductivity of water. The Colburn *j*-factor was calculated using:

$$j = \frac{Nu}{Re \cdot Pr^{0.4}}$$

where *Pr* is the Prandtl number. The thermal performance factor (*TPF*) formula used was:

$$TPF = \frac{Nu}{Nu_o}\frac{f_o}{f}$$

where the subscript *o* corresponds to the vertical pipe serving as a benchmark and friction factor *f* was calculated with the Darcy-Weisbach formula:

$$f = \frac{\Delta P \cdot D}{\rho \cdot \langle U \rangle^2 \cdot L}$$

where $\Delta P/L$ was extracted for each level based on the static pressure contour plots (Fig. A2). Specifically, each level was demarcated based on the axial position at which the static pressure changes significantly. The *Q* criterion was calculated as follows:

$$Q = \frac{1}{2}\left(\mathrm{Tr}(\Omega^T\Omega) - \mathrm{Tr}(S^T S)\right) = \frac{1}{2}\left(\| \Omega\|^2 - \| S\|^2\right)$$
$$= \frac{1}{2}\left(2\left(\omega_{xy}^2 + \omega_{xz}^2 + \omega_{yz}^2\right) - 2\left(s_{xy}^2 + s_{xz}^2 + s_{yz}^2\right) + s_{xx}^2 + s_{yy}^2 + s_{zz}^2\right)$$

where Ω is vorticity tensor defined with vorticity components in three directions $\left(\omega_{ij} = \frac{1}{2}\left(du_i dx_j - du_j dx_i\right)\right)$ and S is strain rate tensor defining with strain rates in all three directions $(s_{ij} = \frac{1}{2}\left(du_i dx_j + du_j dx_i\right))$. Finally, helicity was calculated using

$$helicity = \vec{u} \cdot \vec{\omega} = [u\ v\ w] \cdot \begin{bmatrix} \omega_x \\ \omega_y \\ \omega_z \end{bmatrix}$$

where u, v, and w are velocity components for each direction and $\vec{\omega}$ is vorticity vector.

3. Results and discussion

3.1. Model validation

The Nusselt numbers (*Nu*) and friction factors (*f*) were compared against reported correlations (Table 1) for a vertical pipe (height = 48.6 mm) across the *Re* range of interest in this study. The boundary conditions are inlet temperature of 295.15 K and outlet gauge pressure of 0 Pa. Fig. 2 presents Nusselt number and friction factor as functions of Reynolds number, affirming agreement between the simulated results and the correlations.

Mesh independence tests were performed for the 36° three-level trifurcation model. For mesh size, the effect of hexahedron meshes with pre-adaptation minimum dimensions ranging from $2 \times 10^{-4} - 2 \times 10^{-2}$ mm and maximum dimensions ranging from $1 \times 10^{-2} - 1 \times 10^{2}$ mm was assessed. Through prismatic adaptation (Fig. A1), the y^+ values in the high-gradient wall regions were constrained to below 1 (Table A1).

Fig. 3a presents the area-weighted mean *Nu* directly extractable from Ansys with respect to the number of cells. As the number of cells increased, the area-weighted mean *Nu* for the whole system increased then plateaued beyond 3×10^6 cells, indicating 5.8×10^6 cells as a reasonable threshold for mesh independence. Furthermore, an additional validation using PRESTO! for pressure discretization revealed 0.1 % of deviation in the area-weighted *Nu* when the number of cells was at 5.8×10^6. Additionally, noting the distinctly different local behaviors induced by the junctions, mesh independence was verified axially along the setup. Fig. 3b shows the axial *Nu* profiles resulting from different cell numbers. Clearly, the junctions caused peaks in the *Nu* values. While the profile resulting from 0.7×10^6 cells is obviously different, the trends for cell numbers above 1.3×10^6 cells become similar, affirming mesh independence at and above 5.8×10^6 cells. Moreover, mesh independence for the temperature profiles in regions of marked variations was assessed. Fig. 3c shows the temperature profiles along a chord traversing the *xy*-plane at 1 cm below the top junction, demonstrating mesh independence beyond 1.3×10^6 cells. Fig. 3d displays the temperature profiles across the pipe cross-section at the mid-point of the middle level, similarly reflecting agreement of profiles beyond 1.3×10^6 cells. Table A2 further lists the area-weight mean *Nu*, area-weighted mean surface *h*, and temperature differential (T_{out} - T_{in}) obtained via different number of meshes for the 36° model.

3.2. Heat transfer

Building on the earlier studies on leveraging branching angle to optimize flow by avoiding dead-zones and minimizing pressure drop [15,16,30,31], the impact of branching angle on heat transfer was investigated for the 3D models (Figs. 1b and c).

Fig. 4 depicts the axial temperature profiles for the different

Table 1
Reported correlations for Nusselt numbers (Nu) and friction factors (f).

Parameter	Correlation [a]	Ref
Nu	$Nu = 0.012\ (Re^{0.87} - 280)Pr^{0.4}$	[32]
Nu	$Nu = 0.027\ Re^{0.8}\mathrm{Pr}^{1.3}\left(\frac{\mu}{\mu_w}\right)^{0.14}$	[33]
Nu	$Nu = 0.0275\ Re^{0.8}Pr^{0.385}\left(\frac{L}{D}\right)^{-0.0054}\left(\frac{\mu}{\mu_w}\right)^{0.14}$	[34]
f	$f = 0.316\ Re^{-0.25}$	[35]
f	$f = (1.821 \log(Re) - 1.64)^{-2}$	[36]

[a] Properties of water used for simulations: $\mu = 0.97$ mPa·s; $\rho = 0.997\frac{\mathrm{g}}{\mathrm{cm}^3}$; $\lambda = 0.6\frac{\mathrm{W}}{\mathrm{mK}}$; $c_p = 4.18$ J/kg.

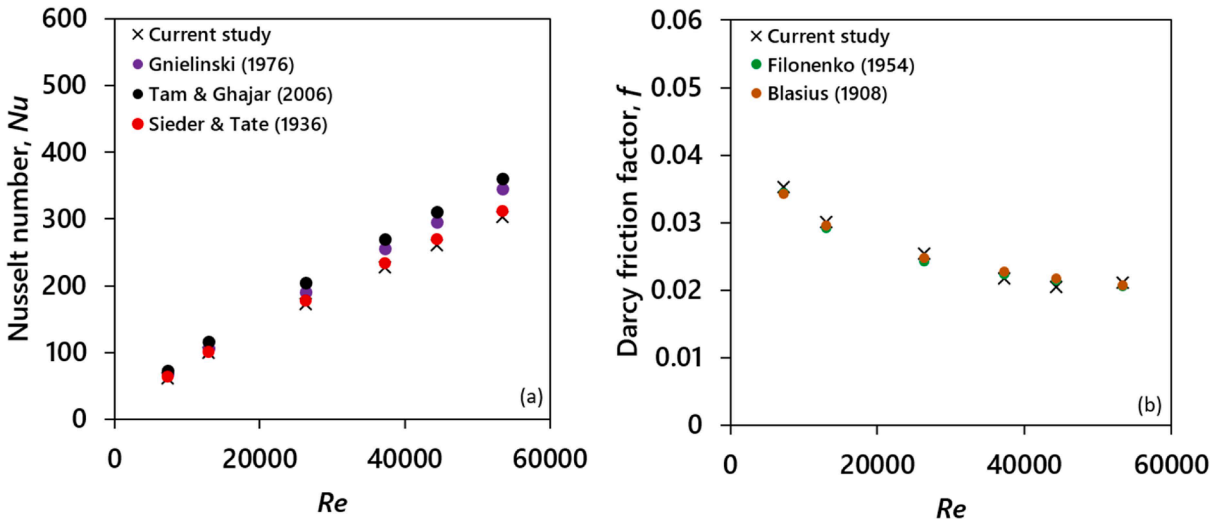

Fig. 2. Comparison numerical results with empirical correlations for a vertical pipe (height = 540 mm, inner diameter = 48.6 mm) across the *Re* range of interest.

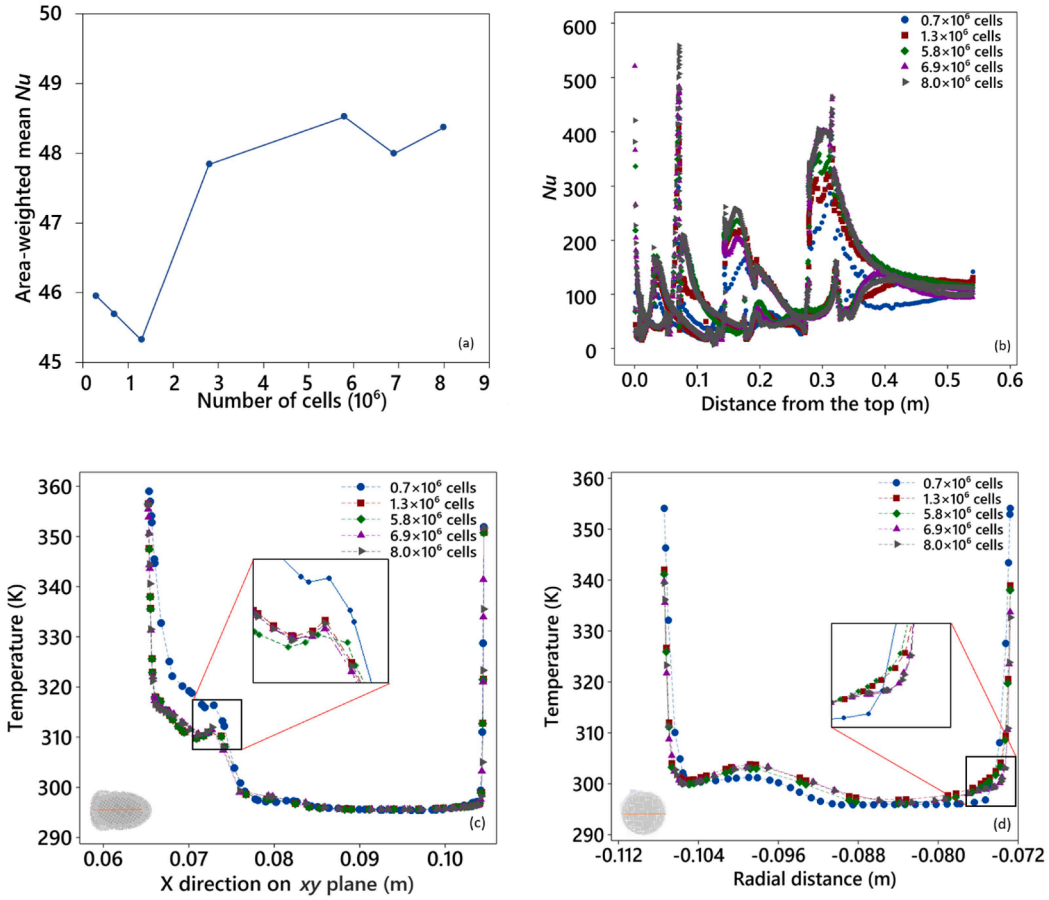

Fig. 3. Mesh independence test for the 36° model: (a) Area-weighted mean Nu for the whole setup with respect to number of cells; (b) Nu in radial-centered axial plane with respect to height; (c) Temperature profiles on xy-plane at 1 cm below the top junction; and (d) Pipe cross-sectional radial temperature profiles at the mid-point of the middle level.

branching models vis-à-vis the conventional vertical pipe. The temperature at the outlet increases as the branching angle decreases, which is due to the increasing wall areas and the fixed wall temperature of 360 K. Notably, while the temperature change along the height is approximately linear for the vertical pipe, steep increases in temperatures are apparent at the junctions for the branching models. At each junction, flows from three pipes converge into a single pipe, giving rise to acceleration and deceleration dynamics that impact heat transfer.

Fig. 5 shows the *Nu* contour plots for the four branched models vis-à-vis a single vertical pipe. For the vertical pipe (Fig. 5e), the *Nu* values are the highest at the entrance and remain low throughout the rest of the pipe. In contrast, for the branching models (Fig. 5a - d), variations in *Nu* throughout the setups are significant. The upper *Nu* limit decreases with angle due to the decrease in the inlet mass flow rate to achieve the same

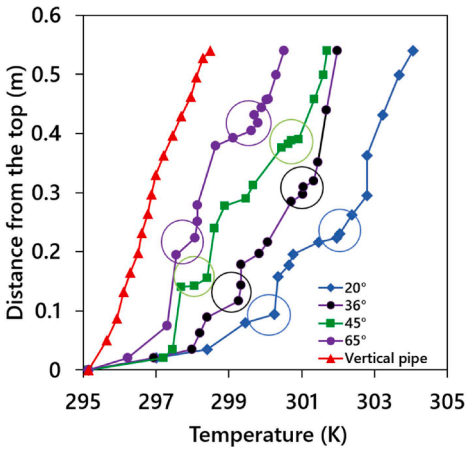

Fig. 4. Mass-weighted mean temperatures versus axial distance, with circles indicating the junctions.

residence time. Also, for all the branching models, the *Nu* values increase from the top level to the bottom level due to the increased flow rates. Notably, the junctions clearly induce higher *Nu* values because of the flow convergence into fewer pipes. Two observations are worth highlighting for the middle level. Firstly, the widest ranges of *Nu* values are near the top junctions for the models with branching angles between 20° – 45°, whereas that for the widest 65° angle is further away from the top junction. This implies the junctions of smaller angles promote non-uniform *Nu* values immediately, while those of the widest angle exert a more delayed effect on the spread of *Nu* values. Secondly, the spread of *Nu* values diminishes approximately monotonically downward of the top junctions for the smaller angles of 20° and 36°, but diminishes to a very narrow range of *Nu* values about midway before increasing again for the wider angles of 45° and 65°. This suggests continuous deceleration of the flow in the middle level for the narrower angles, but a confluence of acceleration and deceleration effects caused by the top and bottom junctions for the wider angles. Therefore, Fig. 5 highlights the distinctly different heat transfer behaviors caused by the different angles. Since the *Re* values are different, Table A3 lists the *Nu/Re* values in the middle level to allow for a fairer comparison of heat transfer efficiency. Among the models, the highest mean *Nu/Re* values and lowest ratio of standard deviation to mean of the *Nu/Re* values (i.e., spread of *Nu/Re* values) in the middle level corresponds to the intermediate angle of 45°, highlighting the non-monotonic relationship between branching angle and heat transfer efficiency.

Fig. 6 presents the Colburn *j*-factor with respect to *Re* for the different models. For each branching model, the three discrete data points represent the three different levels, with the lowest and highest *Re* values corresponding to the top and bottom levels, respectively. On the other hand, for the vertical pipe, the three data points represent three simulations run at different *Re* values, which serve as benchmarks on the heat transfer efficiency of the branching models. Interestingly, among the branching models, the *j* values are the most similar in the middle level, suggesting the flow restrictions caused by the top and bottom junctions of such branching models impact the heat transfer. Nonetheless, the 36° model gives a distinctly higher *j* factor, implying the branching angle and level height can be judiciously designed to enhance heat transfer. At the top level, relative to the vertical pipe, the intermediate angles of 36° and 45° exhibit higher *j* values, whereas the smallest 20° and largest 65° give lower ones, indicating the non-monotonic relationship between heat transfer and branching angle. At the bottom level, the *j* values decrease monotonically as the angle of

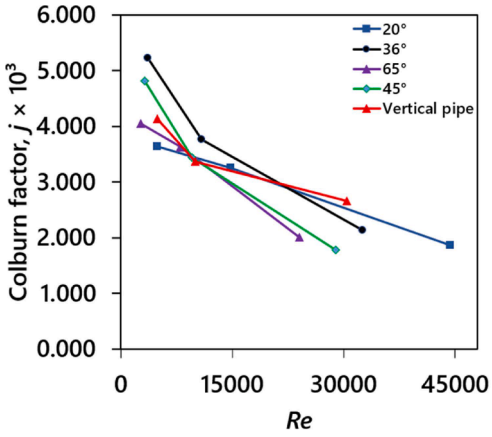

Fig. 6. Colburn j-factor (j) versus *Re* for the different branching angles vis-à-vis vertical pipe. The three data points for each branching model correspond to each level. The three data points for the vertical pipe correspond to three simulations run at different *Re* values.

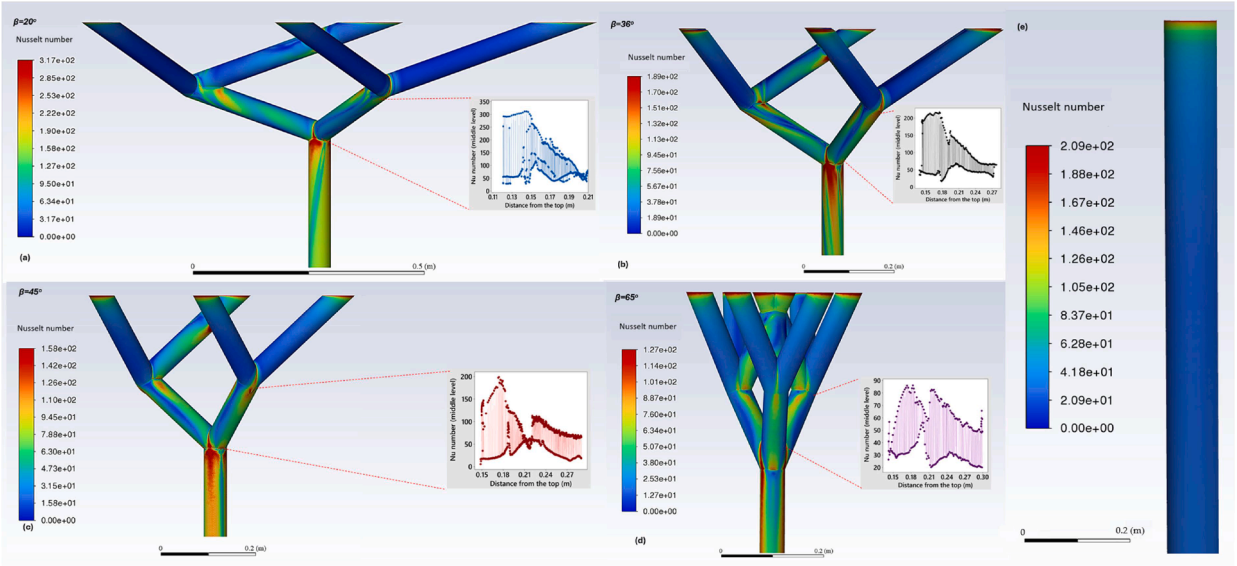

Fig. 5. Nu contour plots in radial-center plane (zero values are removed) for the four branching angles β: (a) 20°; (b) 36°; (c) 45°; and (d) 65°; vis-à-vis (e) a single vertical tube. The inset figures illustrate the variations of Nu values along the middle level.

branches increases.

Fig. 7a presents the thermal performance factor normalized with respect to *Re* (TPF/*Re*), which characterizes the heat transfer enhancement relative to a vertical pipe. A TPF value of less than and greater than 1 implies respectively lower and higher thermal performance than a vertical pipe. Fig. A3 shows that only the middle level of the 20° model has a TPF value of greater than 1. For the larger angles of 45° and 65°, the entire systems exhibit TPF values of less than 0.4, indicating much poorer performance relative to a vertical pipe. Particularly for the top level, all the TPF values are below 0.1. Among the angles, Fig. 7a shows that the average TPF/*Re* (i.e., arithmetic average of the three levels) is the highest and lowest for the intermediate angles of 36° and 45°, respectively. This is directly linked to the corresponding TPF/*Re* values in the middle level, since the TPF/*Re* values are similar for all angles in the top and bottom levels. The marked difference among the angles in the middle level contrasts with the similar j-values in the middle level (Fig. 6), which is because TPF additionally considers the pressure drop through the friction factor (f).

Accordingly, to assess the trade-off between heat transfer effectiveness and flow resistance, Fig. A3b presents *j/f* versus *Re*, while Fig. 7b presents *j/(f·Re)* versus branching angle. Fig. A3b shows the vertical pipe has the highest *j/f*, indicating a more efficient heat exchanger design with lower energy consumption for pumping. Nonetheless, among the branching models, the middle levels of the 20° and 36° models exhibit *j/f* values that approach that of the vertical pipe, suggesting that systematic designs of such levels that lie in between the smaller-angle junctions can be advantageous. The trends for *j/(f·Re)* versus branching angle in Fig. 7b are similar to that for TPF/*Re* (Fig. 7a), with the top and bottom levels giving similar *j/(f·Re)* values among the angles, while the middle level giving distinctly different values.

3.3. Flow dynamics

Fig. 8 shows the velocity magnitude contours for the radial-center planes of the different branching models. Clearly, the top junctions exert significant influences on the flow velocities. At the top level, the lower cross-sections of the pipes accelerate as the top junctions are approached, while the upper cross-sections are at relatively lower velocities. Right after the top junctions, due to the convergence of flows from three pipes, the velocities are significantly augmented at the lower cross-sections, whereas the velocities at the upper walls are approximately stagnant. The bottom levels exhibit the highest velocities due to the further convergence of flows into a single pipe.

Fig. 9 presents the turbulent viscosity (μ_t) contours of the different branching angle models, with the corresponding mesh volume - weighted values for the overall setups listed in Table A4. Clearly, the junctions exert different turbulence patterns depending on the branching angle. At the top levels, the turbulent viscosities are most significantly elevated for the largest 65° model, while least for the 36° model. As for the middle level, the turbulent viscosities appear elevated to different extents and distributions for the different models. To allow for fairer comparison among the angles in view of the different *Re* values, Table 2 lists the means, standard deviations, coefficients of variance (CV), skewness (γ_1), and kurtosis (α_4) of the μ_t/Re values for the middle level. The highest and lowest mean μ_t/Re values are for the 65° and 36° models, respectively, while the greatest spread of values (reflected by ratio of standard deviation to mean) is for the 45° model. Comparing this trend with Fig. 7 suggests that the highest TPF/*Re* and *j/(f·Re)* values (or highest TPF and *j/f* values in Fig. A3) in the middle level corresponding to the 36° model are tied to the lowest μ_t/Re values. This implies heat transfer is enhanced with minimal turbulent dissipation, which suggests the reliance on coherent structures rather than chaotic turbulence to promote heat transfer. In addition, the lowest TPF/*Re* and *j/(f·Re)* values in the middle level corresponding to the 45° model are tied to the greatest spread of the μ_t/Re values. This suggests an inefficient and highly non-uniform heat transfer with poor energy utilization due to flow separation and/or recirculation zones caused by the 45° angle.

Fig. 10 presents the histograms of normalized vorticity *(ΩU/D)* for the middle levels of each branched model, highlighting the distinctly different distributions for the different models. The vorticity contour plots can be found in Fig. A4, while the magnitudes are listed in Tables A5 and A6. The histograms are right-skewed for the smaller angles of 20° and 36°, bimodal for the 45° model, and approximately normal for the 65° model. Also, the highest and lowest *ΩU/D* means are for 36° and 20°, respectively. Interestingly, the 36° model gives the highest mean normalized vorticity (*ΩU/D*) but the lowest mean normalized turbulent viscosity (μ_t/Re), which suggests the fluid motion in the middle level is dominated by organized rotation rather than chaotic, dissipative turbulence. These coherent vortices imply the possibility to leverage the 36° angle to induce the higher TPF values (Fig. 7a). Furthermore, the helicity contour plots in Fig. A4 shows the higher helicity values for the 36° model, indicating organized helical

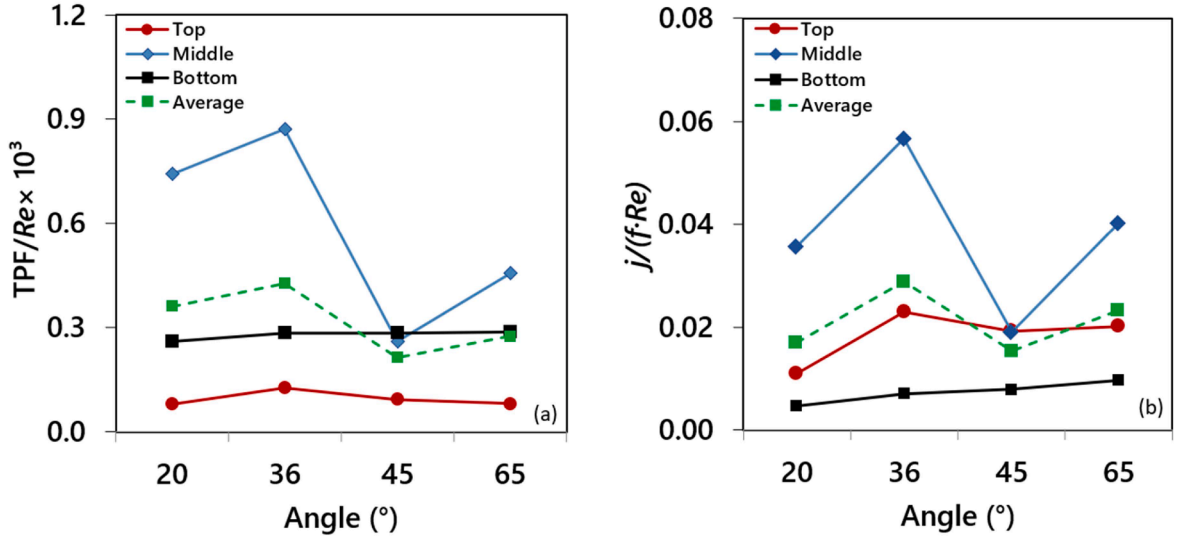

Fig. 7. (a) TPF/*Re* and (b) j/(f·*Re*) versus angle for each level in the different branching angles. The TPF was assessed with respect to a vertical pipe. The averages shown are arithmetic averages of the TPF or j/(f·*Re*) values of the three levels for each angle.

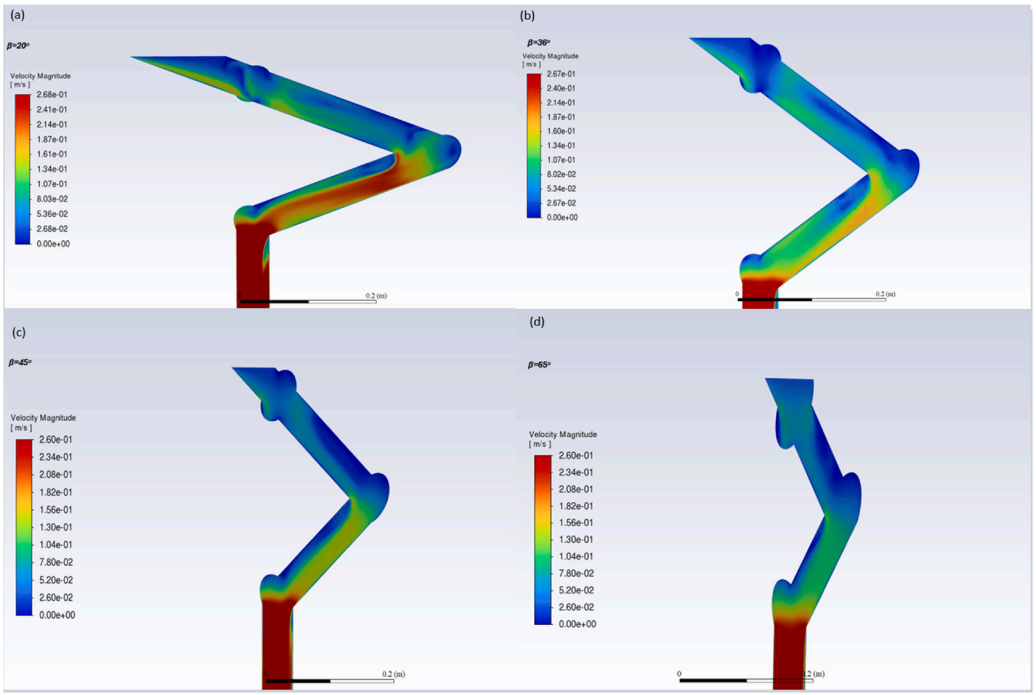

Fig. 8. Velocity magnitude contours in the radial-center planes for the different branching models: (a) 20°; (b) 36°; (c) 45°; and (d) 65°.

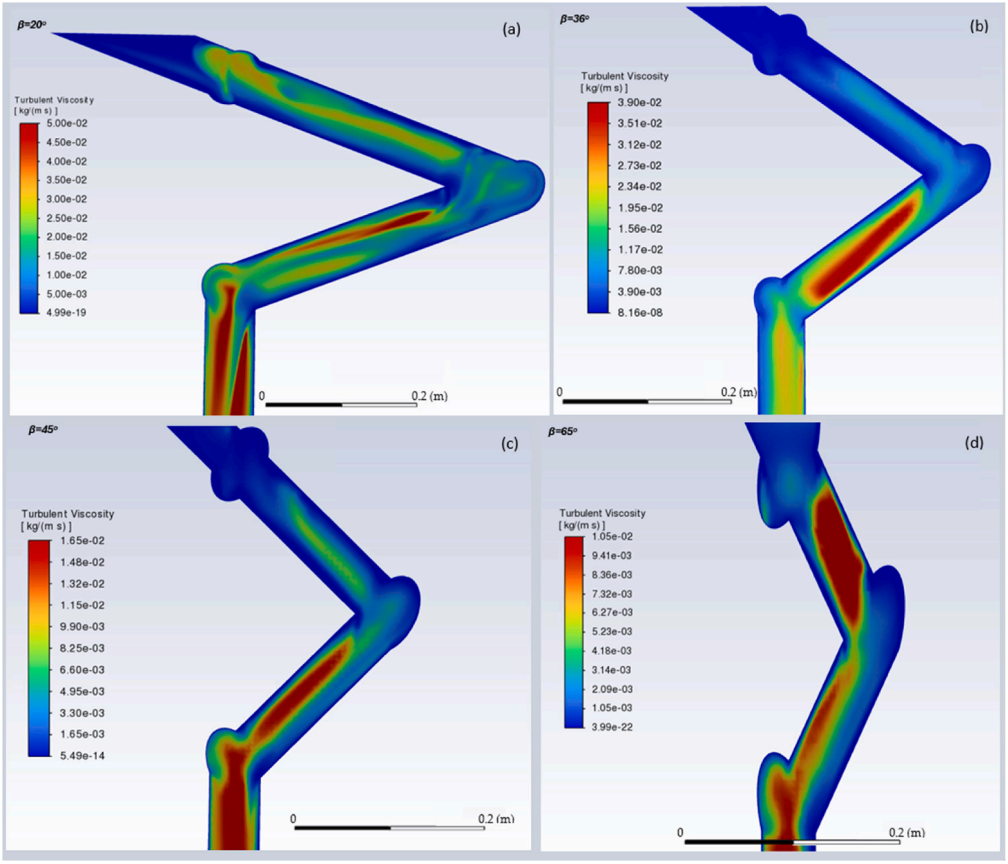

Fig. 9. Turbulent viscosity contours in the radial-center planes for the different branching models: (a) 20°; (b) 36°; (c) 45°; and (d) 65°.

Table 2
μ_t/Re results for the middle level. StDev, CV, γ_1, and α_4 stand for standard deviation, coefficient of variance, skewness, and kurtosis, respectively.

	20°	36°	45°	65°
Mean·10^{13} (kg/m s)	4.59	0.92	4.18	28.3
StDev·10^{12} (kg/m s)	0.95	0.19	1.68	8.34
CV	2.07	2.07	4.05	29.51
γ_1	9.63	6.11	11.37	5.52
α_4	150.54	66.40	179.1	36.47

motion. Coupling high vorticity and high helicity (Fig. A5), the 36° model gives stability and energy efficiency, agreeing with the optimized angle in nature [27].

Fig. 11 shows the turbulent viscosity contour plots of pipes in the top level for each branching model, with the corresponding magnitudes are listed in Table A7. Clearly, the outer and central pipes exhibit different turbulent viscosities, which agrees with earlier studies [12,37]. Consistently for all models, the central pipes exhibit higher turbulent viscosity values than the outer ones. Among the models, the 36° model gives the greatest similarity between the outer and central pipes, the uniformity of which is tied to the low μ_t/Re, high $\Omega/(U/D)$ and high TPF/Re in the middle level.

4. Conclusions

By systematically mimicking nature-evolved designs, the efficiency of engineering designs can be significantly augmented [2]. In this study, the focus is on the ubiquitous heat exchanger. Instead of the conventional vertical pipe, tree-branching designs were considered, since tree branches have evolved to be highly efficient in heat and mass transfer. Accordingly, 3D three-level, trifurcation pipe networks with different branching angles in the range of 20° and 65° were investigated.

While a vertical pipe gives a linear increase in temperature axially, for the branched models, the junctions at which the pipes converge causes steep increases in temperatures. Among the different angles, the heat transfer and flow behaviors are distinctly different between the two junctions (i.e., at the middle level). Interestingly, the relevant parameters characterized are largely non-monotonic with respect to angle. Notably, the 36° model results in the highest *Re*-normalized thermal performance factor (TPF/*Re*), highlighting the superior performance of this intermediate angle, which agrees with past studies [27]. Investigation of the flow behavior reveals the lowest mean normalized turbulent viscosity (μ_t/Re) and highest mean normalized vorticity ($\Omega U/D$). The dominance of coherent flow structures governing the efficient heat transfer suggests the possibility to systematically leverage the 36° angle to further augment heat transfer, for example by using changing the pipe length for the middle level or number of branches.

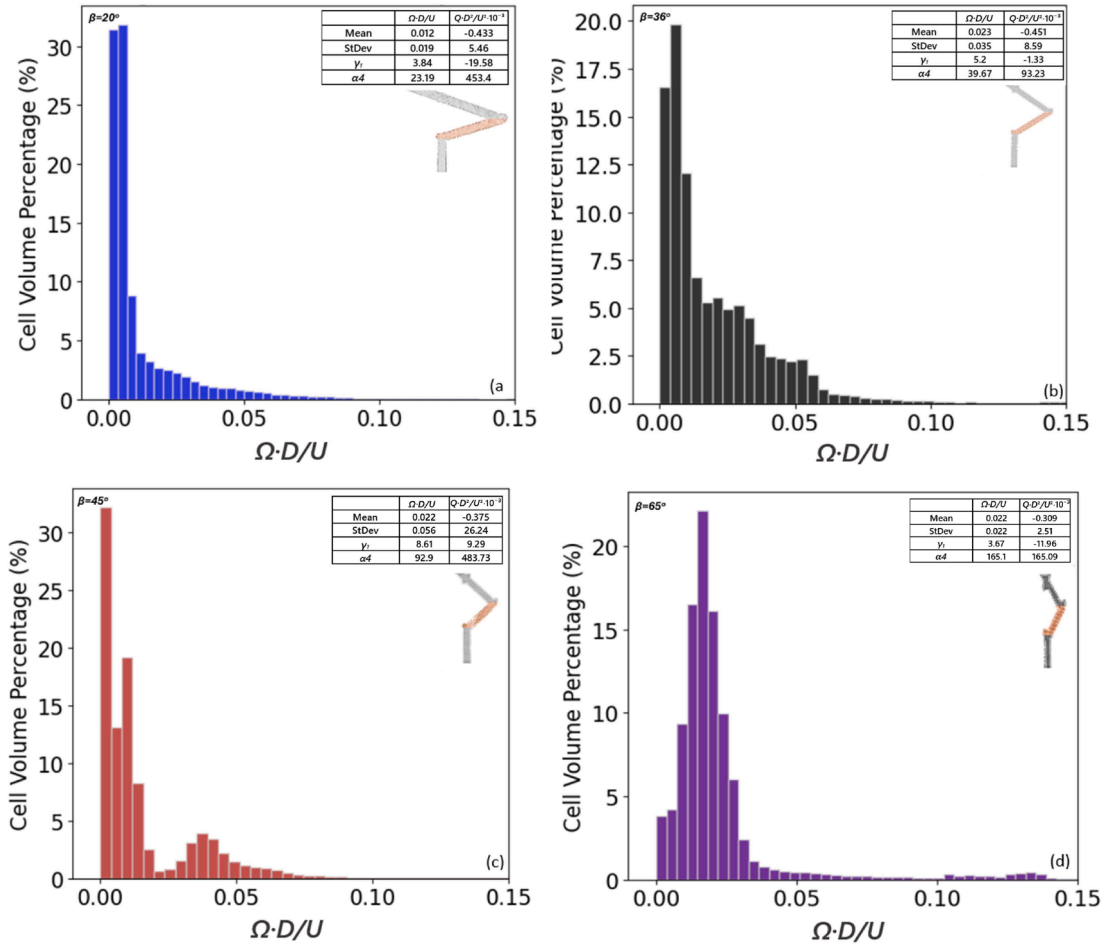

Fig. 10. Vorticity normalized by D/U (ΩU/D) histograms for the middle levels of the branching angles: (a) 20°; (b) 36°; (c) 45°; and (d) 65°.

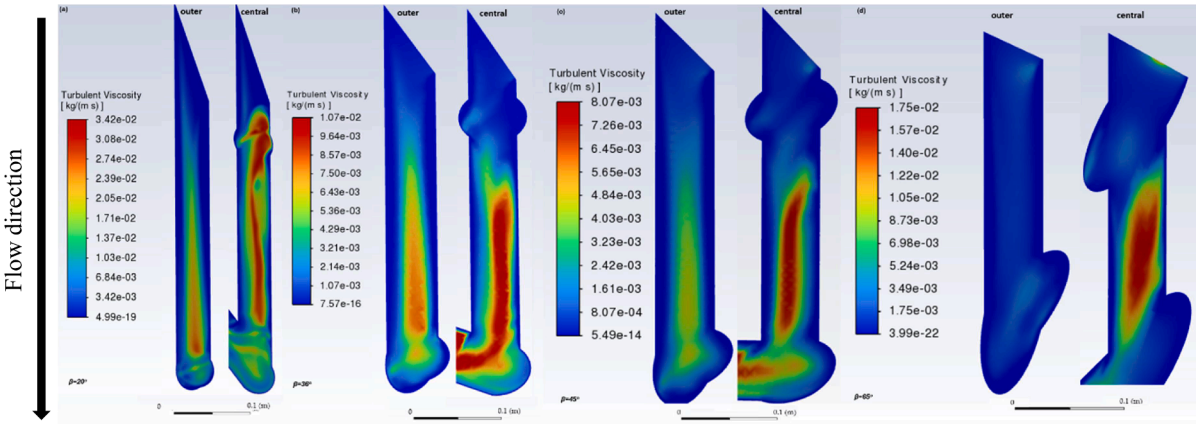

Fig. 11. Turbulent viscosity contours in the radial-center planes of the outer and central pipes in the top level for the different branching angles: (a) 20°; (b) 36°; (c) 45°; and (d) 65°.

The results here are expected to be valuable for optimizing heat exchanger performance based on systematic mimicry of natural tree branches. It should be noted that our goal here was to clarify the potential of these branching architectures rather than claim them as ready replacements for conventional exchangers, given the associated operational complexities and capital costs. From a cleaning standpoint, such exchangers are most compelling in sealed low-fouling loops (e.g., battery or electronics cold-plate cooling) [38], or in aerospace systems (e.g., regeneratively cooled rocket engines) where maintenance may rely on module swap-out rather than cleaning [39]. As additive manufacturing continues to lower lead time and cost, if superior performance can be demonstrated to adequately offset additional costs, branching designs may offer practical advantages.

CRediT authorship contribution statement

Aladdin Mardanov: Writing – original draft, Visualization, Validation, Methodology, Investigation, Formal analysis. **Ronnie Andersson:** Writing – review & editing, Validation, Supervision, Methodology. **Jia Wei Chew:** Writing – review & editing, Validation, Supervision, Resources, Project administration, Methodology, Investigation, Funding acquisition, Formal analysis, Conceptualization.

Declaration of competing interest

The authors declare that they have no known competing financial interests or personal relationships that could have appeared to influence the work reported in this paper.

Acknowledgement

This work was supported by Chalmers Gender Initiative for Excellence (Genie).

Appendix

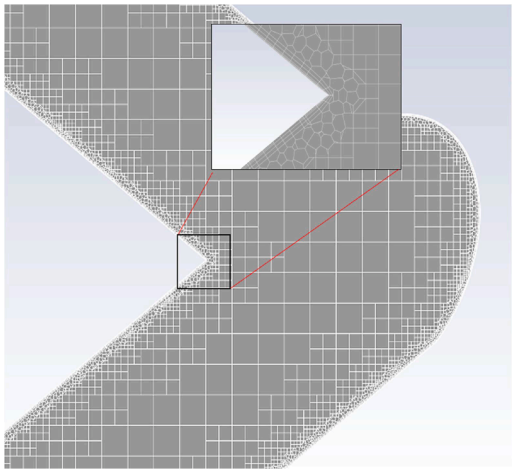

Fig. A1. Mesh size in critical regions resulting from increased number of meshes and mesh adaption. Inner pipe diameter is 48.6 mm.

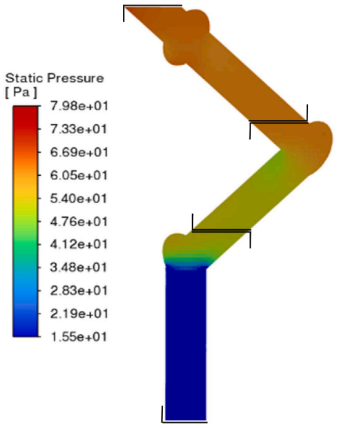

Fig. A2. Static pressure contour plot of the 45° model, with additional exact locations between which $\Delta P/L$ was obtained.

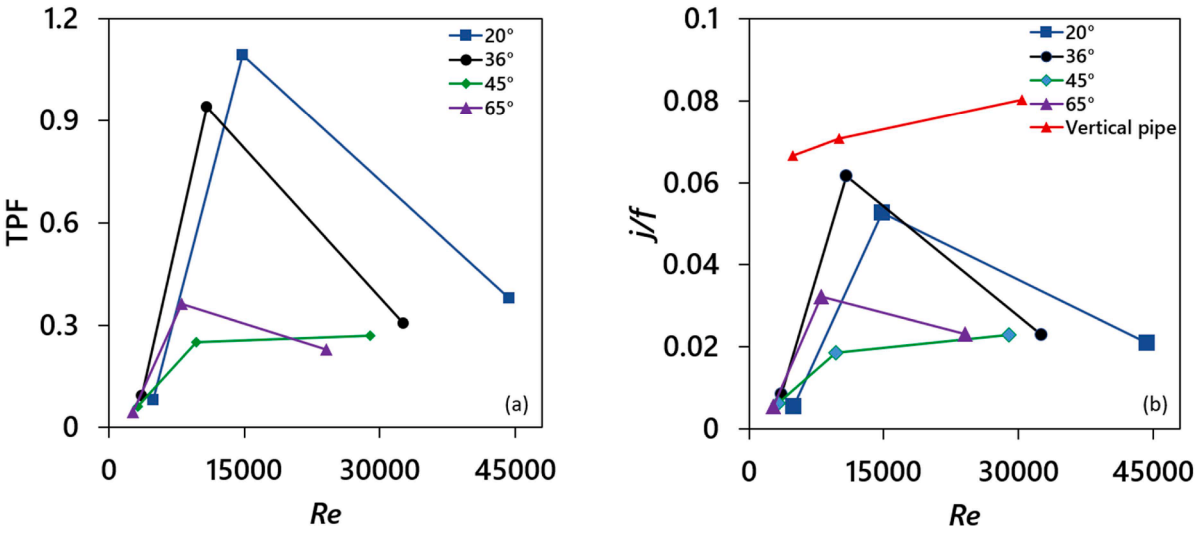

Fig. A3. (a) TPF versus *Re*; and (b) *j/f* versus *Re*.

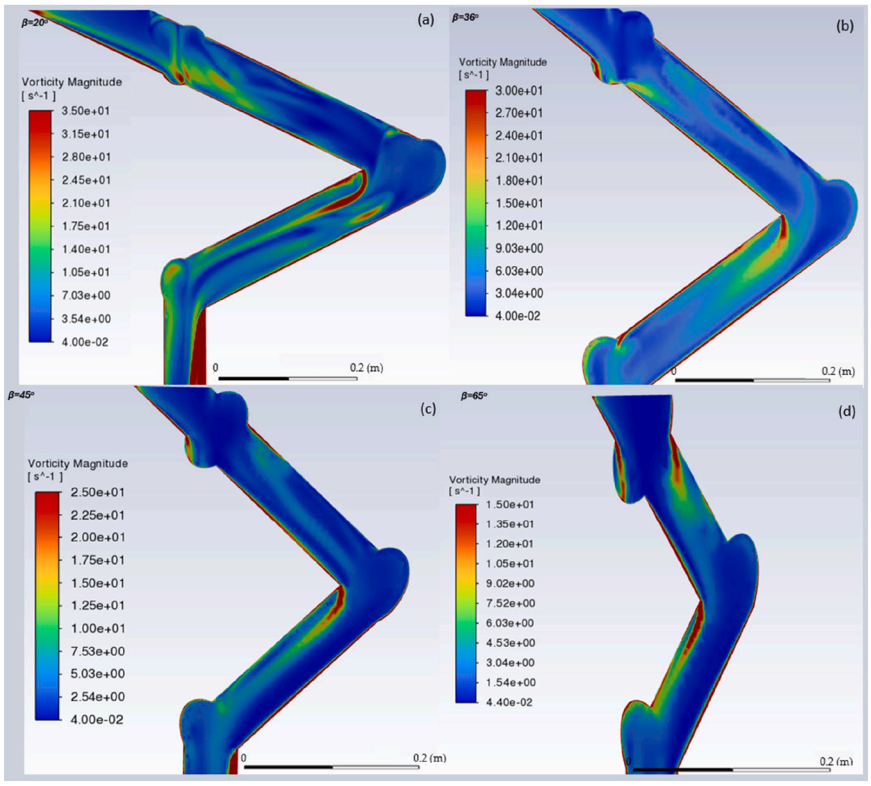

Fig. A4. Vorticity contours of the central plane for the branched models: (a) 20°, (b) 36°, (c) 45°, and (d) 65°.

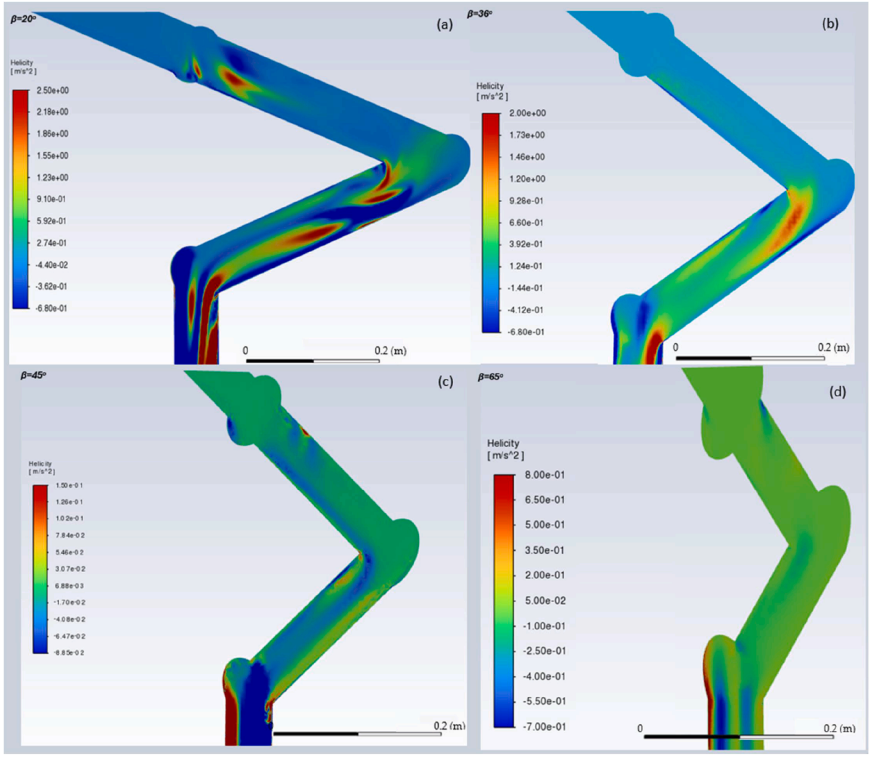

Fig. A5. Helicity contours of the central plane for the branched models: (a) 20°, (b) 36°, (c) 45°, and (d) 65°.

Table A1
Y^+ values for the models with different branching angles and the vertical pipe (90°).

Angle	Min	Max	Mean
20°	0.018	0.921	0.42
36°	0.031	0.897	0.52
45°	0.045	0.992	0.43
65°	0.005	0.997	0.63
90°	0.500	0.989	0.68

Table A2
Effect of mesh number on various parameters of the 36° model. Area-weighted mean Nu, surface heat transfer coefficient, and global temperature change of water based on different number of meshes for the same CAD model.

Number of meshes	Area-weighted mean *Nu*	Area-weighted mean surface *h* (W/m^2K)	T_{out}-T_{in} (K)
3×10^5	45.94	559.93	7.10
7×10^5	45.69	556.82	8.13
1.3×10^6	45.32	582.40	7.40
2.8×10^6	47.84	587.82	8.58
5.8×10^6	48.52	590.21	8.63
6.9×10^6	47.99	584.89	8.57
8×10^6	48.37	589.49	8.62

Table A3
Nu/*Re* results for the middle level. StDev, CV, γ_1, and α_4 stand for standard deviation, coefficient of variance, skewness, and kurtosis, respectively.

Angle	Mean•10^{-2}	StDev•10^{-2}	StDev/Mean	γ_1	α_4
20°	9.58	5.03	0.52	1.77	3.09
36°	8.67	4.70	0.54	0.98	2.03
45°	12.9	5.64	0.44	0.42	−0.19
65°	8.46	4.25	0.50	1.28	3.07

Table A4
Mesh volume - weighted turbulent viscosity (kg/m s) for the overall setups. StDev, IQR, γ_1, and α_4 stand for standard deviation, interquartile range, skewness, and kurtosis, respectively.

Angle	Mean	StDev	Variance	Median	Maximum	IQR	γ1	α4
20°	6.78E-09	1.40E-08	1.96E-16	0.009124	0.072614	0.021951	12.6	158.59
36°	9.98E-10	2.13E-09	4.53E-18	0.000667	0.040582	0.003562	6.65	69.65
45°	4.02E-09	1.63E-08	2.64E-16	0.000001	0.025686	0.00031	11.77	159.56
65°	2.27E-08	6.69E-08	4.49E-15	0.000534	0.017916	0.002525	6.5	46.23

Table A5
Vorticity (s^{-1}) magnitudes in the radial-center planes of the entire setups. StDev, CV, IQR, γ_1, and α_4 stand for standard deviation, coefficient of variance interquartile range, skewness, and kurtosis, respectively.

Vorticity									
Angle	Mean	StDev	Variance	CV	Minimum	Maximum	IQR	γ_1	α_4
20°	35.25	307.47	94,539.26	336.48	0.48	9299.58	21.62	7.94	111.28
36°	50.78	198.56	39,427.56	235.92	0.33	3521.56	54.33	5.2	46.36
45°	134.9	334.6	111,924.7	190.39	0.23	10,961.1	182.5	10.76	226.67
65°	21.63	86.9	7551.85	232.88	0.028	1398.55	23.66	4.71	34.54

Table A6
Vorticity magnitude (s^{-1}) in the top and middle levels. Values were taken from the entire setup. StDev, CV, γ_1, and α_4 stand for standard deviation, coefficient of variance, skewness, and kurtosis, respectively.

Top Level Angle	Mean	StDev	Variance	CV	γ_1	α_4
20°	45.09	59.18	3502.57	336.48	3.33	15.51
36°	47.12	48.59	2361.66	235.92	2.11	7.04
45°	25.73	32.24	1039.18	190.39	6.29	85.68
65°	17.77	20.9	439.43	232.88	4.58	34.14
Middle Level						
Angle	**Mean**	**StDev**	**Variance**	**CV**	**γ_1**	**α_4**
20°	76.31	117.42	13,786.58	336.48	3.84	23.19
36°	106.73	158.46	25,109.47	235.92	5.33	39.94
45°	94.29	235.64	55,525.52	190.39	8.28	85.89
65°	21.63	86.9	5737.53	232.88	3.67	15.02

Table A7
Turbulent viscosity (kg/m s) in the radial-center planes of the inner and outer branches of the top level. StDev, CV, IQR, γ_1, and α_4 stand for standard deviation, coefficient of variance interquartile range, skewness, and kurtosis, respectively.

	Angle	Mean	StDev	Variance	CV	Min.	IQR	Max.	γ_1	α_4
Central	**20°**	0.07E-09	0.046376	0.002151	64.17	0	0.078336	0.168243	0.25	−1.04
	36°	0.01E-10	0.000907	0.000001	315.55	0	0.000119	0.008536	5.45	34.09
	45°	0.01E-09	0.000512	0.000001	285.74	0	0.000076	0.004618	4.8	27.52
	65°	0.01E-09	0.000537	0.000001	163.22	0	0.000458	0.003743	2.05	4.53
Outer	**20°**	0.007929	0.009275	0.000086	107.66	0	0.014798	0.031975	0.88	−0.46
	36°	0.000517	0.001622	0.000003	202.2	0	0.000768	0.011719	3.56	14.42
	45°	0.000382	0.001088	0.000001	191.78	0	0.000599	0.00854	3.87	18.07
	65°	0.001061	0.002859	0.000008	186.89	0	0.001367	0.017916	2.82	8.41

Data availability

Data will be made available on request.

References

[1] Z. Huang, Y. Hwang, R. Radermacher, Review of nature-inspired heat exchanger technology, Int. J. Refrig. 78 (2017) 1–17, https://doi.org/10.1016/j.ijrefrig.2017.03.006.

[2] M.-O. Coppens, Nature-inspired chemical engineering for process intensification, Annu Rev. Chem. Biomol. Eng. 12 (2021) 187–215, https://doi.org/10.1146/annurev-chembioeng-060718-030249. Volume 12, 2021.

[3] P. Trogadas, M.-O. Coppens, Chapter 2 - nature-inspired chemical engineering: a new design methodology for sustainability, in: G. Szekely, A. Livingston (Eds.), Sustainable Nanoscale Engineering, Elsevier, 2020, pp. 19–31, https://doi.org/10.1016/B978-0-12-814681-1.00002-3.

[4] A. Bejan, G. Tsatsaronis, M. Moran, Thermal Design and Optimization, Wiley, New York, 1996.

[5] N.M. Donald, Tree and Networks in Biological Models, Wiley, Chichester, 1983.

[6] Z. Stankovic, B.D. Allen, J. Garcia, K.B. Jarvis, M. Markl, 4D flow imaging with MRI, Cardiovasc. Diagn. Ther. 4 (2) (2014) 173–192, https://doi.org/10.3978/j.issn.2223-3652.2014.01.02.

[7] G.J. Hademenos, T.F. Massoud, Biophysical mechanisms of stroke, Stroke 28 (10) (1997) 2067–2077, https://doi.org/10.1161/01.str.28.10.2067.

[8] Z. Zhu, J. Li, H. Peng, D. Liu, Nature-Inspired Structures Applied in Heat Transfer Enhancement and Drag Reduction, Micromachines. (Basel) 12 (6) (2021), https://doi.org/10.3390/mi12060656.

[9] A.M. Aragón, J.K. Wayer, P.H. Geubelle, D.E. Goldberg, S.R. White, Design of microvascular flow networks using multi-objective genetic algorithms, Comput. Methods Appl. Mech. Eng. 197 (49) (2008) 4399–4410, https://doi.org/10.1016/j.cma.2008.05.025.

[10] M. Saber, J.-M. Commenge, L. Falk, Rapid design of channel multi-scale networks with minimum flow maldistribution, Chem. Eng. Process.: Process Intensif. 48 (3) (2009) 723–733, https://doi.org/10.1016/j.cep.2008.09.001.

[11] S. Kalisz, M. Pronobis, Influence of non-uniform flow distribution on overall heat transfer in convective bundle of circulating fluidized bed boiler, Heat Mass Transf. 41 (11) (2005) 981–990, https://doi.org/10.1007/s00231-004-0608-3.

[12] H. Liu, P. Li, Even distribution/dividing of single-phase fluids by symmetric bifurcation of flow channels, Int. J. Heat. Fluid. Flow. 40 (2013) 165–179, https://doi.org/10.1016/j.ijheatfluidflow.2013.01.011.

[13] Y. Chen, P. Cheng, Heat transfer and pressure drop in fractal tree-like microchannel nets, Int. J. Heat. Mass Transf. 45 (13) (2002) 2643–2648, https://doi.org/10.1016/S0017-9310(02)00013-3.

[14] H. Sakaguchi, Reaction-diffusion-advection equation in binary tree networks and optimal size ratio, Phys. Rev. E 90 (4) (2014) 040801, https://doi.org/10.1103/PhysRevE.90.040801.

[15] S.A. Marzouk, M.M. Abou Al-Sood, E.M.S. El-Said, M.M. Younes, M.K. El-Fakharany, Evaluating the effects of bifurcation angle on the performance of a novel heat exchanger based on contractual theory, Renew. Energy 219 (2023) 119463, https://doi.org/10.1016/j.renene.2023.119463.

[16] E. Davydova, S. Deridder, S. Eeltink, G. Desmet, P.J. Schoenmakers, Optimization and evaluation of radially interconnected versus bifurcating flow distributors using computational fluid dynamics modelling, J. Chromatogr. A 1380 (2015) 88–95, https://doi.org/10.1016/j.chroma.2014.12.063.

[17] X.-B. Liu, Q. Chen, M. Wang, N. Pan, Z.-Y. Guo, Multi-dimensional effect on optimal network structure for fluid distribution, Chem. Eng. Process.: Process Intensif. 49 (10) (2010) 1038–1043, https://doi.org/10.1016/j.cep.2010.07.006.

[18] F. Ma, Z. Zeng, Y. Gao, E. Liu, J. Xue, Research status and progress of bionic surface drag reduction, China Surface Eng. 29 (1) (2016) 7–15.

[19] W. Lin, C. J, X. Fang, Z. Zhang, Research progress of heat transfer enhancement of shell-and-tube heat exchanger, Chem. Ind. Eng. Prog. 37 (2018) 1276–1286.

[20] F. Ma, Z. Zeng, Y. Gao, E. Liu, J. Xue, Research status and progress of bionic surface drag reduction, China Surface Eng. 29 (2016) 7–15.

[21] X. Huang, W. Yang, T. Ming, W. Shen, X. Yu, Heat transfer enhancement on a microchannel heat sink with impinging jets and dimples, Int. J. Heat. Mass Transf. 112 (2017) 113–124, https://doi.org/10.1016/j.ijheatmasstransfer.2017.04.078.

[22] S.M. Gleason, C.J. Blackman, S.T. Gleason, K.A. McCulloh, T.W. Ocheltree, M. Westoby, Vessel scaling in evergreen angiosperm leaves conforms with Murray's law and area-filling assumptions: implications for plant size, leaf size and cold tolerance, New Phytologist 218 (4) (2018) 1360–1370, https://doi.org/10.1111/nph.15116.

[23] E. Rosenberg, On deriving Murray's law from constrained minimization of flow resistance, J. Theor. Biol. 512 (2021) 110563, https://doi.org/10.1016/j.jtbi.2020.110563.

[24] C. Xia, J. Fu, J. Lai, X. Yao, Z. Chen, Conjugate heat transfer in fractal tree-like channels network heat sink for high-speed motorized spindle cooling, Appl. Therm. Eng. 90 (2015) 1032–1042, https://doi.org/10.1016/j.applthermaleng.2015.07.024.

[25] A. Bejan, Advanced Engineering Thermodynamics, third ed., Wiley, New Jersey, 2006.

[26] A. Bejan, Convection Heat Transfer, third ed., Wiley, New York, 2004.

[27] A. Bejan, L.A.O. Rocha, S. Lorente, Thermodynamic optimization of geometry: T- and Y-shaped constructs of fluid streams, Int. J. Therm. Sci. 39 (2000) 949–960.

[28] L. Ghodoossi, Conceptual study on constructal theory, Energy Convers. Manage 45 (9) (2004) 1379–1395, https://doi.org/10.1016/j.enconman.2003.09.002.
[29] S. Zhang, Y. Lu, Y. Gu, X. Zhang, J. Sun, Z. Tang, The process intensification of CO2 absorption in honeycomb fractal reactor fabricated by 3D printer, Chem. Eng. Process. - Process Intensif. 132 (2018) 42–47, https://doi.org/10.1016/j.cep.2018.08.013.
[30] A. Bejan, L.A.O. Rocha, S. Lorente, Thermodynamic optimization of geometry: T- and Y-shaped constructs of fluid streams, Int. J. Thermal Sci. 39 (9) (2000) 949–960, https://doi.org/10.1016/S1290-0729(00)01176-5.
[31] J. Cao, M. Kraut, R. Dittmeyer, L. Zhang, H. Xu, Numerical analysis on the effect of bifurcation angle and inlet velocity on the distribution uniformity performance of consecutive bifurcating fluid flow distributors, Int. Commun. Heat Mass Transf. 93 (2018) 60–65.
[32] V. Gnielinski, New equations for heat and mass transfer in turbulent pipe and channel flow, Int. Chem. Eng. 16 (2) (1976) 359–367.
[33] E.N. Sieder, G.E. Tate, Heat transfer and pressure drop of liquids in tubes, Ind. Eng. Chem. 28 (12) (1936) 1429–1435, https://doi.org/10.1021/ie50324a027.
[34] L.M. Tam, A.J. Ghajar, Transitional heat transfer in plain horizontal tubes, Heat Transf. Eng. 27 (5) (2006) 23–38, https://doi.org/10.1080/01457630600559538.
[35] H. Blasius, Grenzschichten in Flussigkeiten mit kleiner, Reibung. Eng. transl, NACA TM 1256 (1908).
[36] G.K. Filonenko, Hydraulic resistance in pipes, Teploenergetika 1 (4) (1954) 40–44.
[37] P. Li, D. Coopamah, N. Dhar, Analysis and optimization of flow distribution channels for uniform flow in fuel cells, in: ASME 2008 Fluids Engineering Division Summer Meeting collocated with the Heat Transfer, Energy Sustainability, and 3rd Energy Nanotechnology Conferences, 2008, pp. 915–920.
[38] G. Zhao, X. Wang, M. Negnevitsky, C. Li, An up-to-date review on the design improvement and optimization of the liquid-cooling battery thermal management system for electric vehicles, Appl. Therm. Eng. 219 (2023) 119626, https://doi.org/10.1016/j.applthermaleng.2022.119626.
[39] F. Careri, R.H.U. Khan, C. Todd, M.M. Attallah, Additive manufacturing of heat exchangers in aerospace applications: a review, Appl. Therm. Eng. 235 (2023) 121387, https://doi.org/10.1016/j.applthermaleng.2023.121387.